RESEARCH ARTICLE | JANUARY 27 2025

Transport properties of h-BN lateral devices

G. Somasundaram ; A. Tingsuwatit ; Z. Alemoush ; J. Li ; J. Y. Lin ; H. X. Jiang

Appl. Phys. Lett. 126, 043502 (2025)
https://doi.org/10.1063/5.0241120

Applied Physics Letters ARTICLE pubs.aip.org/aip/apl

Transport properties of h-BN lateral devices

Cite as: Appl. Phys. Lett. **126**, 043502 (2025); doi: 10.1063/5.0241120
Submitted: 28 September 2024 · Accepted: 16 January 2025 ·
Published Online: 27 January 2025

G. Somasundaram, A. Tingsuwatit, Z. Alemoush, J. Li, J. Y. Lin, and H. X. Jiang[a]

AFFILIATIONS

Department of Electrical and Computer Engineering, Texas Tech University, Lubbock, Texas 79409, USA

[a]Author to whom correspondence should be addressed: hx.jiang@ttu.edu

ABSTRACT

One of the well-established and significant applications of hexagonal boron nitride (h-BN) is in solid-state neutron detectors, which necessitate the development of quasi-bulk h-BN crystals. To advance the material and device development of h-BN, it is essential to characterize its bulk electrical transport properties. However, this task is challenging due to h-BN's ultrawide bandgap (UWBG) of approximately 6.1 eV, which results in an extremely high electrical resistivity, typically exceeding 10^{12} Ω·cm. On the other hand, the mobility-lifetime ($\mu\tau$) product, a key figure of merit for determining the overall device performance, is more readily accessible through the characterization of the I-V characteristics under illumination. In this study, we investigate the in-plane $\mu\tau$ products of lateral devices fabricated from freestanding quasi-bulk h-BN wafers synthesized by hydride vapor phase epitaxy. Our results reveal an unexpected decrease in the in-plane $\mu\tau$ product as the device width decreases. Utilizing a simple two-region carrier transport model, where the central region of the device represents the bulk h-BN material free from metal contacts and the two edge regions are influenced by metal contacts, we demonstrate that the $\mu\tau$ product in the edge areas covered by metal contacts decreases by nearly two orders of magnitude compared to the bulk value. We attribute this significant reduction in $\mu\tau$ product to the layered crystalline structure of h-BN, which permits metal atoms to infiltrate into the interlayer spacings. As a result, the measured $\mu\tau$ product is significantly lower than the true bulk value. These findings provide valuable insights into the design and fabrication of high-performance h-BN devices, which typically leverage its exceptional in-plane transport properties.

Hexagonal boron nitride (h-BN) has garnered considerable attention as a platform for constructing novel two-dimensional structures, including graphene-based heterostructures,[1,2] and for hosting optically stable single-photon emitters.[3] Much of the research in this area has focused on monolayers or few-layer h-BN, typically obtained through exfoliation methods that rely on millimeter-sized bulk crystals grown via high-pressure, high-temperature (HPHT) techniques[4–7] and metal flux solution methods.[8,9] However, these approaches present significant challenges in scaling up to larger wafer and device sizes. As a semiconductor, h-BN is particularly appealing for a variety of advanced applications due to its exceptional physical properties. These include an ultrawide energy bandgap (UWBG) of approximately 6.1 eV,[4–6,10,11] a measured breakdown field of around 12 MV/cm,[7] and calculated in-plane electron and hole mobilities of μ_e ~120 $cm^2/V{\cdot}s$ and μ_h ~440 $cm^2/V{\cdot}s$, respectively.[12] Additionally, h-BN exhibits a measured in-plane thermal conductivity of about 550 W/m·K.[9] These remarkable bulk properties contribute to very high figures of merit (FOM) for electronic and photonic devices, which could significantly broaden the advanced applications of III-nitride semiconductors in areas such as lighting and consumer electronics,[13–18] power electronics,[19–22] full-spectrum solar energy conversion,[23–25] and UV sterilization and curing technologies.[26–28] In this context, advancing crystal growth and device technologies to process large-diameter, thick epitaxial films (or quasi-bulk wafers) with high crystalline quality is crucial for harnessing the full potential of h-BN in advanced semiconductor device applications. The initial active device that requires the use of h-BN quasi-bulk crystals demonstrated so far is the high-efficiency thermal neutron detectors.[29,30]

Notably, h-BN is exceptionally well suited for the fabrication of direct conversion solid-state neutron detectors.[29–32] This advantage primarily stems from the presence of boron-10 (B-10), one of the few isotopes with a favorable nuclear interaction cross section for thermal neutrons, measuring 3840 barns.[33,34] This results in an absorption length for thermal neutrons of 47 μm in B-10 enriched h-BN and 237 μm in natural h-BN.[29–32] These substantial absorption lengths underscore the importance of developing h-BN quasi-bulk wafers to achieve high-efficiency thermal neutron detectors.

We have fabricated 1 cm^2 thermal neutron detectors using 100 μm thick B-10 enriched h-BN quasi-bulk wafers, achieving a record thermal neutron detection efficiency of 60%. This accomplishment is enabled by the significant wafer thickness, which provides an absorption of 88% for thermal neutrons [calculated as 1-exp(−100/47)], and by leveraging the superior lateral transport properties of h-BN. This was achieved through the integration of multiple narrow

lateral detectors, each measuring 1.3 mm in width, to effectively collect neutron-generated charge carriers.[29,30,32]

In order to pave the way for the industrial adoption of h-BN detector technologies, there is a need to further enhance the device performance as well as manufacturing yield. One straightforward approach is to incorporate lateral detectors with increased widths without compromising carrier transport properties. However, the inherently high electrical resistivity of h-BN presents challenges in measuring and understanding its electrical transport characteristics. For instance, traditional Hall effect measurement techniques, which are standard for assessing the electrical transport properties of semiconductors, are difficult to apply to these UWBG materials. Nevertheless, the ability to measure and comprehend the carrier transport properties is essential for advancing h-BN as a viable UWBG electronic material.

Despite these challenges, the high electrical resistivity of h-BN naturally results in extremely low dark currents, facilitating ease in characterization of the bias dependence of photocurrent (or the photocurrent–voltage characteristics under illumination). By analyzing these characteristics, the charge carrier mobility-lifetime products ($\mu\tau$), one of the most critical parameters for determining device performance, can be obtained using the classical Many's equation developed for highly resistive semiconductors.[35–37] This method of characterizing $\mu\tau$ has been effectively employed to guide the development of h-BN quasi-bulk crystal growth as well as h-BN neutron detectors by monitoring advancements in the $\mu\tau$ products.[29–32] This approach is analogous to solar cells, where the absorption coefficient and $\mu\tau$ product are key figures of merit influencing overall performance.[38,39] Over the past decade, the $\mu\tau$ products of our h-BN materials have improved by several orders of magnitude from 10^{-8} – 10^{-9} cm^2/V[31] to $> 10^{-4}$ cm^2/V.[29,30,32] In this study, we carried out studies of the in-plane charge carrier transport properties of h-BN lateral devices with varying device widths to provide an improved understanding of lateral transport properties and valuable insights into realizing high performance h-BN devices.

The freestanding h-BN quasi-bulk wafer used here was synthesized using hydride vapor phase epitaxy (HVPE) growth technique using natural boron trichloride (BCl_3) and ammonia (NH_3) as precursors for B and N, respectively.[30] HVPE is a well-established method for producing quasi-bulk GaN crystals in large wafer sizes at high growth rates. Recently, HVPE technique has been utilized to produce GaN vertical p-n junction devices, achieving significantly better p-type conductivity control by eliminating residual carbon impurities.[40,41] The growth of h-BN was carried out on 4″-diameter c-plane sapphire substrates at a temperature of 1500 °C. Due to the layered structure of h-BN, the material naturally separated from sapphire during the cooling process after completing growth, resulting in a freestanding wafer, as shown in Fig. 1(a). As shown in Fig. 1(b), x-ray diffraction (XRD) 2θ-ω scan revealed a (002) peak at 26.72°, corresponding to a c-lattice constant of nearly 6.66 Å,[30] whereas the transmission electron microscope (TEM) measurement provided a direct measure of the spacing between the stacked planes (or c/2) in the c-direction of 3.33 Å,[42] consistent with the expected c-lattice constant of pure h-BN.

To study the in-plane charge carrier transport properties, lateral devices of different widths were fabricated from the same wafer and placed in the same electronic package, as shown in Fig. 2(a). It is important to highlight that the absorption length of thermal neutrons in natural h-BN is 237 μm, which means that neutron-generated charge carriers are distributed throughout the bulk of the detector material.[29–32] Consequently, the metal contacts must extend across the entire vertical edges of the detector to ensure that the electric field is uniformly applied in the c-plane throughout the bulk of the detector material. This uniform electric field is crucial for the effective collection of neutron-generated charge carriers from the entire volume of the detector. This is in contrast to the scenario in two-dimensional h-BN devices[43] as well as in thin epitaxial h-BN detectors,[31] where all contacts are deposited on one surface. Given the extremely high electrical resistivity of h-BN, depositing metal contacts solely on the top surface of the h-BN results in the electric field being concentrated only near the surface beneath the contact, which inhibits the collection of neutron-generated charge carriers that are located deeper within the device.

In light of these considerations, the device fabrication process was carried out in the following steps: (1) h-BN strips measuring 10 mm × 1.3 mm, 10 mm × 2.4, and 10 mm × 4.0 mm were cut from the h-BN quasi-bulk wafer and spin-coated onto the surface of a sapphire wafer; (2) a shadow mask with corresponding dimensions, featuring an overlapping area of 100 μm on each side, was employed to deposit metal contacts on the two edges of the h-BN devices; (3) a 100 nm thick nickel (Ni) layer was deposited, followed by a 40 nm

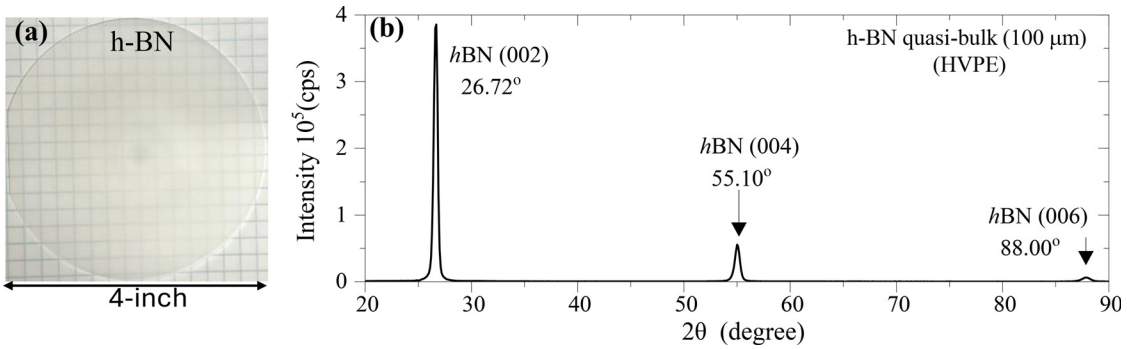

FIG. 1. (a) Image of the 4″-diameter freestanding h-BN quasi-bulk wafer used in this study. (b) XRD pattern in $2\theta - \omega$ scan from 20°–90° of a 100 μm thick freestanding and flexible h-BN quasi-bulk wafer synthesized by hydride vapor phase epitaxy (HVPE). Figure reproduced from Ref. 30 under the terms of the Creative Commons CC BY license, Alemoush *et al.*, J. Appl. Phys. 135, 175704 (2024).

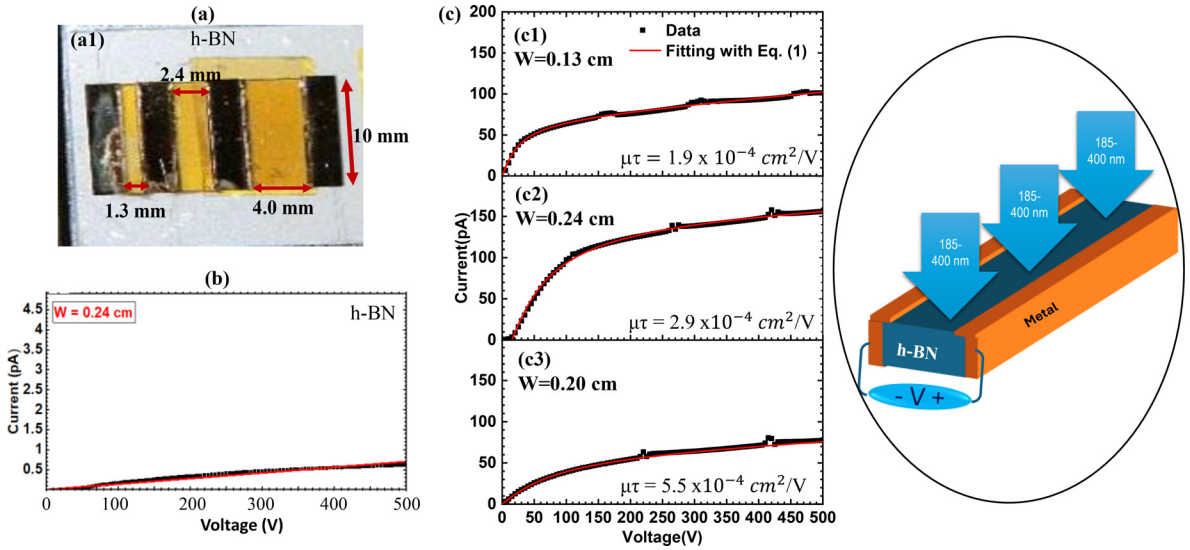

FIG. 2. (a) Image of packaged h-BN lateral devices showing different widths (W = 1.3, 2.4, and 4.0 mm). (b) I–V characteristics of the 2.4 mm wide device measured in the dark. (c) Measured applied voltage dependence of photocurrent (solid dots) and least squares fitting using Eq. (1) (red curves) for three lateral devices with varying widths of (c1) W = 0.13 cm, (c2) W = 0.24 cm, and (c3) W = 0.4 cm. The inset is a schematic of experimental setup for measuring the I–V characteristics under illumination by a broad light source covering from 185 to 400 nm.

thick gold (Au) layer through the openings in the shadow mask using electron-beam (e-beam) deposition; and (4) wire bonding was subsequently utilized to connect the metal contacts to a device package, facilitating electrical characterization. During the metal deposition process, we observed that when metal contacts were deposited along the edges of h-BN in a direction parallel to the c-plane, the contacts become shorted. This is due to the layered crystalline structure of h-BN, allowing metal atoms to infiltrate into the interlayer spacings, giving rise to a channeling effect. To address this issue, we tilted the samples at approximately 20 degrees to ensure that the metal contacts adequately cover the entire edges of the h-BN devices.

As shown in Fig. 2(b), the electrical resistivity of these h-BN devices was determined by measuring the I–V characteristics in the dark, yielding a resistivity of around 5×10^{12} Ω·cm. The charge carrier mobility-lifetime product ($\mu\tau$) dictates the transport properties and ability for charge carrier collection in h-BN devices. In order to ensure an effective collection of the radiation-generated charge carriers by the electrodes, the recombination or capture lifetime (τ) of the carriers must exceed the transit time (τ_t), meaning $\tau \geq \tau_t$. The transit time of the charge carriers can be expressed as the transit distance divided by the velocity (μE) of the charge carriers. Thus, the charge collection condition can also be written as $\mu\tau$ E $\gg$ W, or equivalently $\frac{\mu\tau V}{W^2} \gg 1$, where E (V) denotes the electric field (bias voltage) applied to the lateral device. At a fixed W, the required bias voltage for providing an effective charge collection is inversely proportional to $\mu\tau$. On the other hand, for a given value of $\mu\tau$ product, the required bias voltage to support an effective charge collection scales with W^2.

The bias voltage dependence of the photocurrent was measured under illumination by a low-pressure mercury lamp with excitation wavelengths covering from 185 to 400 nm, as illustrated in the inset shown in the right panel of Fig. 2(c). Figure 2(c) plots the measured I-V characteristics under illumination for three lateral devices with varying widths of (c1) W = 0.13 cm, (c2) W = 0.24 cm, and (c3) W = 0.4 cm. The red curves in Fig. 2 are the least squares fitting of the measured data using a modified Many's equation by including the effect of a non-complete blocking contacts, i.e., the parameter a is non-zero,[37]

$$I(V) = \left(I_o \mu \frac{\tau V}{W^2}\right)\left[1 - (1-a)\left(\mu\frac{\tau V}{W^2}\right)\left(1 - \exp\left(-\frac{W^2}{\mu\tau V}\right)\right)\right], \quad (1)$$

which provides the $\mu\tau$ products of the devices. The results in Fig. 2(c) yield $\mu\tau = 1.9 \times 10^{-4}$ cm^2/V, 2.9×10^{-4} cm^2/V, and 5.5×10^{-4} cm^2/V for the 1.3, 2.4, and 4 mm wide devices, respectively, while another 2 mm wide device fabricated independently exhibiting a value of $\mu\tau = 2 \times 10^{-4}$ cm^2/V.[44]

It is worth pointing out that we have previously conducted time-of-flight measurements to extract the lateral $\mu\tau$ product in h-BN, and the results were highly consistent with those obtained from the simpler I–V characteristics under photoexcitation measurements.[45] This consistency reinforces our confidence in the reliability of utilizing I-V characteristics under photoexcitation to extract $\mu\tau$ product, which is significantly simpler than the time-of-flight technique. We have also measured the wavelength-dependent photocurrent, also known as the photocurrent excitation spectrum, which provided crucial insights into the band edge structure of h-BN and indicated that the photocurrent is predominantly generated by the band edge excitation.[40] For devices fabricated from another 100 μm thick wafer with a width of 1.3 mm, the $\mu\tau$ product measured using a laser-driven broad-spectrum light source covering a wavelength range of 190–2400 nm, with significantly higher optical power, was 2.28×10^{-4} cm^2/V,[35] which aligns well with the measured value of 1.9×10^{-4} cm^2/V for the 1.3 mm wide device tested with the low-pressure mercury lamp UV light source here, despite the latter using a much lower optical power and different

excitation wavelength range. These comparative results suggest, to the first order, that the $\mu\tau$ product is primarily influenced by the overall quality of the material.

In Fig. 3(a), we plot the measured $\mu\tau$ products for the four devices of different widths, showing that $\mu\tau$ increases with device width (W), which is very surprising, given that $\mu\tau$ is an intrinsic property depending only on the over material quality and is generally considered independent of device dimension. To qualitatively account for the width dependence of $\mu\tau$ product, we propose a two-region carrier transport model. This model consists of a bulk region free from metal deposition and two edge regions that are in contact with metal, as depicted in Fig. 3(b). During the metal deposition process on the edges of h-BN, although we tilted the samples at approximately 20°, some metal atoms can still infiltrate the spaces between the stacked layers near the edges. This occurs due to the layered crystalline structure of h-BN, which adversely affects the transport properties in the edge regions. The detrimental impact is particularly significant in devices with narrower widths, leading to a noticeable reduction in the measured $\mu\tau$ product as the width (W) decreases.

To support our interpretation, as illustrated in Fig. 3(b), we denote the width of the metal contacts on the two edges of the devices by $\Delta/2$ and the width of the central area of the device is then $(w - \Delta)$, where $\Delta/2 = 100\,\mu$m by design. In Fig. 3(b), we denote the mobility-lifetime product in the edge areas by $(\mu\tau)_E$ and in the central area of the device by its bulk value $(\mu\tau)_B$, respectively. It is expected that the $(\mu\tau)_E$ is much smaller than $(\mu\tau)_B$, $(\mu\tau)_E \ll (\mu\tau)_B$. Consequently, the measured $\mu\tau$ product represents the average value between the two, which is anticipated to be smaller than its bulk value, $(\mu\tau) < (\mu\tau)_B$. In contrast, in other UWBG semiconductors, such as AlN, c-BN, and diamond, metal atoms are not expected to infiltrate into the material.

Assuming that the photoexcited charge carriers are generated uniformly, on the average, the charge carriers in the central area of the device travel a distance of $(W/2 - \Delta/2)$, whereas the charge carriers in the edge areas travel a distance of $\Delta/2$. Thus, the transit time of charge carriers generated in the central areas can be expressed as $(W/2 - \Delta/2)/(\mu E)_B$ and in the edge areas as $(\Delta/2)/(\mu E)_E$, whereas the average (effective) transit time of charge carriers is $(W/2)/(\mu E)$. The relationship between three quantities can be described as follows:

$$\frac{W/2}{(\mu E)}\gamma = \frac{W/2 - \Delta/2}{(\mu E)_B}\gamma_B + \frac{\Delta/2}{(\mu E)_E}\gamma_E, \tag{2}$$

which results in

$$\mu\tau = \frac{(\mu\tau)_B(\mu\tau)_E}{(1 - \Delta/W)(\mu\tau)_E + (\Delta/W)(\mu\tau)_B}. \tag{3}$$

Here, γ $(=1/\tau)$, $\gamma_B(=1/\tau_B)$ and $\gamma_E(=1/\tau_E)$ denote the average carrier capture rate, the carrier capture rate in the bulk region, and the carrier capture rate in the two edge regions, respectively. The solid curve in Fig. 3(a) is a plot of Eq. (3) using values of $\Delta = 200\,\mu$m, $(\mu\tau)_B = 3 \times 10^{-3}$ cm^2/V, and $(\mu\tau)_E = 2.3 \times 10^{-5}$ cm^2/V. The applied field in the central and edge areas of the device is assumed to be uniform. However, the measured $\mu\tau$ depends on both the bulk mobility-lifetime product $(\mu\tau)_B$ and edge mobility-lifetime product $(\mu\tau)_E$, as well as the device width W. If $\Delta \ll W$, the edge effects are minimal, and the measured $\mu\tau$ will closely be approaching $(\mu\tau)_B$. Conversely, if Δ is a significant fraction of W, the edge properties $(\mu\tau)_E$ will have a larger influence on the measured $\mu\tau$ product.

The value of the bulk mobility and lifetime product, $(\mu\tau)_B$, obtained from Fig. 3(a) is 3×10^{-3} cm^2/V, which is much larger than the measured value of $(\mu\tau) \sim (1.9 - 5.4) \times 10^{-4}$ cm^2/V. The qualitative agreement between Eq. (3) and the measured data suggests the validity of our simple two-region carrier transport model. The mobility-lifetime product of charge carriers in the edge area $(\mu\tau)_E$ is in

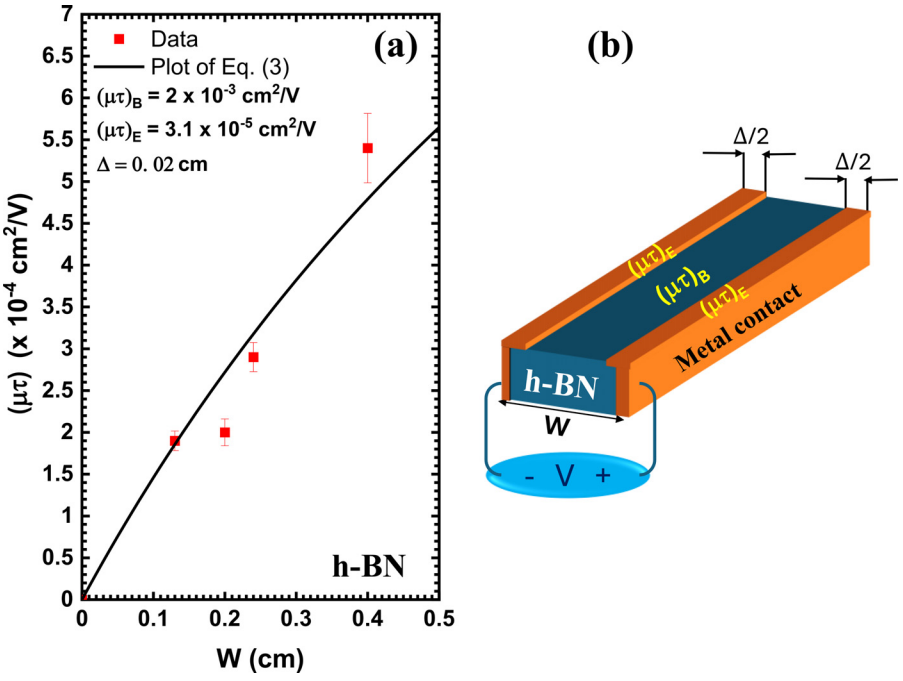

FIG. 3. (a) Measured mobility-lifetime product $(\mu\tau)$ vs device width (W). The solid curve is a plot of Eq. (3) using $\Delta = 200\,\mu$m, $(\mu\tau)_B = 3 \times 10^{-3}$ cm^2/V, and $(\mu\tau)_E = 2.3 \times 10^{-5}$ cm^2/V. (b) Schematic illustration of a h-BN lateral device with metal contacts deposited on the two edges of h-BN, where $(\mu\tau)_B$ denotes the bulk mobility and lifetime product of photogenerated charge carriers in the central region of the device and $(\mu\tau)_E$ denotes the mobility and lifetime product of photogenerated charge carriers near two edges of the device.

the order of 2×10^{-5} cm^2/V, which is nearly two orders of magnitude smaller than the bulk value of 3×10^{-3} cm^2/V, leading to a reduction in the measured $\mu\tau$ product from the true bulk value. However, the measured $\mu\tau$ product, which determines the performance of the device, is expected to further decrease with an increase in the metal contact width (Δ). This point is highlighted in Fig. 4, which plots $\mu\tau$ vs Δ according to Eq. (3) for a 0.4 cm wide device using $(\mu\tau)_B = 5 \times 10^{-3}$ cm^2/V and $(\mu\tau)_E = 1 \times 10^{-5}$ cm^2/V. The results indicate that the measured $\mu\tau$ product can be reduced by nearly one order of magnitude if the contact width on the two edges is increased from 0.006 to 0.06 cm.

Although these results provide only a qualitative description of $\mu\tau$ product dependence on the detector width (W), they have important implications for implementing h-BN as an active device material. For instance, the charge carrier collection condition of $\frac{\mu\tau V}{W^2} \gg 1$ implies that to boost the charge collection efficiency at a given operating voltage (V), reducing the device width (W) is an easier route than enhancing $\mu\tau$ product through optimizing the crystal growth process. However, the analysis presented here stresses that the transport properties of photogenerated charge carriers deteriorate more significantly with metal deposition at the edges for devices with narrower widths, and an effect must be taken into consideration in fabricating h-BN lateral devices. On the other hand, the effect of metal atoms infiltration is less severe in wider detectors, but the required operating voltage for providing an effective charge collection increases with W^2 for a given

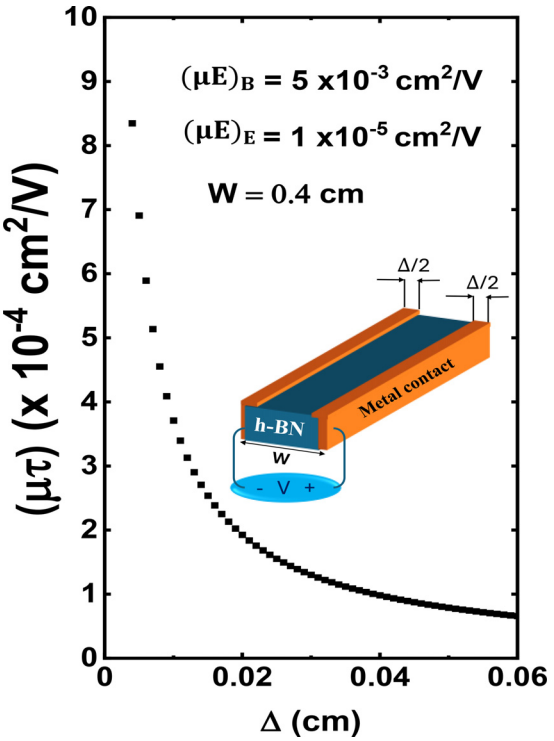

FIG. 4. Plot of $\mu\tau$ vs Δ according to Eq. (3) for a 0.4 cm wide device using $(\mu\tau)_B = 5 \times 10^{-3}$ cm^2/V and $(\mu\tau)_E = 1 \times 10^{-5}$ cm^2/V, illustrating the impact of metal deposition at the edges on the $\mu\tau$ product of h-BN lateral devices. The inset is a schematic illustration of a h-BN lateral device with two metal contacts deposited on the edges each with a width of $\Delta/2$.

$\mu\tau$ product. The results underscore the necessity for ongoing efforts to enhance the overall material quality (or $\mu\tau$ product) of h-BN quasi-bulk crystals to further facilitate the production efficiency of high-performance h-BN lateral devices.

In summary, we report a detailed study on the in-plane charge carrier transport properties of h-BN by probing the charge carrier mobility and lifetime products ($\mu\tau$) of lateral devices with varying widths. Our analysis revealed that the deposition of metal contact at the edges of h-BN devices adversely affects the carrier transport properties, leading to a reduction in the $\mu\tau$ product. This degradation is attributed to metal atoms infiltrating the spacings between the stacked layers of h-BN, a direct consequence of its layered crystalline structure. This observation underscores the significant impact of metal contacts on the device performance, as the measured $\mu\tau$ product was found to be considerably lower than the true bulk value. Our findings provide valuable insights into the lateral transport characteristics of h-BN and highlight the necessity of optimizing metal deposition processes and configurations, with a focus on minimizing the infiltration of metal atoms into the interlayer spaces while preserving the outstanding lateral transport properties of h-BN. Specifically, optimizing these processes is anticipated to enhance the performance of h-BN neutron detectors, which hold potential applications in nuclear energy, national security, nuclear waste monitoring, and materials science. The development of h-BN UWBG semiconductor neutron detectors with high efficiencies is anticipated to unlock unprecedented applications that are unattainable with other types of neutron detectors. Additionally, the progress made in quasi-bulk material growth and device processing so far represents a significant milestone in advancing the technology needed to produce electronic-grade h-BN quasi-bulk crystals, which can serve both as an active host and as substrate material for a wide range of applications, including deep UV photonics, high-power electronics, high-efficiency neutron detectors, and quantum information technology.

The information, data, or work presented herein was funded in part by the Advanced Research Projects Agency-Energy (ARPA-E), U.S. Department of Energy (Award No. DE-AR0001552) monitored by Dr. Olga Spahn and Dr. Eric Carlson. The views and opinions of authors expressed herein do not necessarily state or reflect those of the United States Government or any agency thereof. Jiang and Lin are grateful to the AT&T Foundation for the support of Ed Whitacre and Linda Whitacre endowed chairs.

AUTHOR DECLARATIONS

Conflict of Interest

The authors have no conflicts to disclose.

Author Contributions

G. Somasundaram: Data curation (equal); Formal analysis (equal); Investigation (equal); Methodology (equal); Software (equal); Validation (equal); Visualization (equal); Writing – original draft (equal). **A. Tingsuwatit:** Data curation (equal); Formal analysis (equal); Investigation (equal); Methodology (equal); Software (equal); Validation (equal); Visualization (equal). **Z. Alemoush:** Data curation (equal); Formal analysis (equal); Investigation (equal); Methodology (equal); Software (equal); Validation (equal); Visualization (equal). **J.**

Li: Data curation (equal); Formal analysis (equal); Investigation (equal); Methodology (equal); Project administration (equal); Resources (equal); Software (equal); Supervision (equal); Validation (equal); Visualization (equal). **J. Y. Lin:** Conceptualization (equal); Formal analysis (equal); Funding acquisition (equal); Investigation (equal); Methodology (equal); Project administration (equal); Resources (equal); Supervision (equal); Validation (equal); Visualization (equal); Writing – review & editing (equal). **H. X. Jiang:** Conceptualization (equal); Formal analysis (equal); Funding acquisition (equal); Investigation (equal); Methodology (equal); Project administration (equal); Resources (equal); Supervision (equal); Validation (equal); Visualization (equal); Writing – original draft (equal); Writing – review & editing (equal).

DATA AVAILABILITY

The data that support the findings of this study are available within the article.

REFERENCES

[1]N. Alem, R. Erni, C. Kisielowski, M. D. Rossell, W. Gannett, and A. Zettl, Phys. Rev. B **80**, 155425 (2009).
[2]A. K. Geim and I. V. Grigorieva, Nature **499**, 419 (2013).
[3]R. Bourrellier, S. Meuret, A. Tararan, O. Stephan, M. Kociak, L. H. G. Tizei, and A. Zobelli, Nano Lett. **16**, 4317 (2016).
[4]K. Watanabe, T. Taniguchi, and H. Kanda, Nat. Mater. **3**, 404 (2004).
[5]K. Watanabe and T. Tanniguchi, Phys. Rev. B **79**, 193104 (2009).
[6]G. Cassabois, B. Valvin, and Gil, P., Nat. Photonics **10**, 262 (2016).
[7]Y. Hattori, T. Taniguchi, K. Watanabe, and K. Nagashio, Appl. Phys. Lett. **109**, 253111 (2016).
[8]Y. Kubota, K. Watanabe, O. Tsuda, and T. Taniguchi, Science **317**, 932 (2007).
[9]C. Yuan, J. Li, L. Lindsay, D. Cherns, J. W. Pomeroy, S. Liu, J. H. Edgar, and M. Kuball, Commun. Phys. **2**, 43 (2019).
[10]T. Sugino, K. Tanioka, S. Kawasaki, and J. Shirafuji, Jpn. J. Appl. Phys. **36**(Part 2), L463 (1997).
[11]B. Arnaud, S. Lebègue, P. Rabiller, and M. Alouani, Phys. Rev. Lett. **96**, 026402 (2006).
[12]M. M. Khatami, M. L. Van de Put, and W. G. Vandenberghe, Phys. Rev. B **104**, 235424 (2021).
[13]S. Pimputkar, J. S. Speck, S. P. DenBaars, and S. Nakamura, Nat. Photonics **3**, 180 (2009).
[14]H. Amano, N. Sawaki, I. Akasaki, and Y. Toyoda, Appl. Phys. Lett. **48**, 353 (1986).
[15]S. Nakamura, T. Mukai, and M. Senoh, Appl. Phys. Lett. **64**, 1687 (1994).
[16]M. A. Khan, R. A. Skogman, R. G. Schulze, and M. Gershenzon, Appl. Phys. Lett. **42**, 430 (1983).
[17]H. X. Jiang and J. Y. Lin, Nat. Electron. **6**, 257 (2023).
[18]P. J. Parbrook, B. Corbett, J. Han, T. Y. Seong, and H. Amano, Laser Photonics Rev. **15**, 2000133 (2021).
[19]M. Asif Khan, A. Bhattarai, J. N. Kuznia, and D. T. Olson, Appl. Phys. Lett. **63**, 1214 (1993).
[20]M. Higashiwaki, R. Kaplar, J. Pernot, and H. Zhao, Appl. Phys. Lett. **118**, 200401 (2021).
[21]Y. H. Chen, J. Encomendero, C. Savant, V. Protasenko, H. G. Xing, and D. Jena, Appl. Phys. Lett. **124**, 152111 (2024).
[22]Z. He, X. Zhang, T. S. Pieshkov *et al.*, Appl. Phys. Lett. **125**, 042106 (2024).
[23]J. Wu, W. Walukiewicz, K. Yu, J. W. Ager III, E. E. Haller, H. Lu, W. J. Schaff, Y. Saito, and Y. Nanishi, Appl. Phys. Lett. **80**, 4741 (2002).
[24]S. Vanka, B. Zhou, R. A. Awni, Z. Song, F. A. Chowdhury, X. Liu, H. Hajibabaei, W. Shi, Y. Xiao, I. A. Navid, A. Pandey, R. Chen, G. A. Botton, T. W. Hamann, D. Wang, Y. Yan, and Z. Mi, ACS Energy Lett. **5**, 3741 (2020).
[25]Y. Zhao, M. Xu, X. Huang *et al.*, Mater. Today Energy **31**, 101229 (2023).
[26]A. Khan, K. Balakrishnan, and T. Katona, Nat. Photonics **2**, 77 (2008).
[27]Y. Taniyasu, Kasu, T, and Makimoto, M., Nature **441**, 325 (2006).
[28]Z. Zhang, M. Kushimoto, T. Sakai, N. Sugiyama, L. J. Schowalter, C. Sasaoka, and H. Amano, Appl. Phys. Express **12**, 124003 (2019).
[29]A. Maity, S. J. Grenadier, J. Li, J. Y. Lin, and H. X. Jiang, Appl. Phys. Lett. **116**, 142102 (2020).
[30]Z. Alemoush, A. Tingsuwatit, A. Maity, J. Li, J. Y. Lin, and H. X. Jiang, J. Appl. Phys. **135**, 175704 (2024).
[31]T. C. Doan, S. Majety, S. Grenadier, J. Li, J. Y. Lin, and H. X. Jiang, Nucl. Instrum. Methods Phys. Res., Sect. A **748**, 84 (2014).
[32]A. Maity, S. J. Grenadier, J. Li, J. Y. Lin, and H. X. Jiang, Prog. Quantum. Electron. **76**, 100302 (2021).
[33]O. Osberghaus, Z. fuer Phys. **128**, 366 (1950).
[34]G. F. Knoll, *Radiation Detection and Measurement*, 4th ed. (John Wiley & Sons, 2010).
[35]A. Many, J. Phys. Chem. Solids **26**, 575 (1965).
[36]U. Lachish, Nucl. Instrum. Methods Phys. Res., Sect. A **403**, 417 (1998).
[37]A. Tingsuwatit, N. K. Hossain, Z. Alemoush, M. Almohammad, J. Li, J. Lin, and Y. Jiang, Appl. Phys. Lett. **124**, 162105 (2024).
[38]N. Beck, N. Wyrsch, C. Hof, and A. Shah, J. Appl. Phys. **79**, 9361 (1996).
[39]P. Kaienburg, L. Krückemeier, D. Lübke, J. Nelson, U. Rau, and T. Kirchartz, Phys. Rev. Res. **2**, 023109 (2020).
[40]H. Fujikura, K. Taichiro, K. Takeshi, N. Yoshinobu, and H. Fumimasa, Appl. Phys. Lett. **117**, 012103 (2020).
[41]K. Ohnishi, F. Naoki, N. Shugo, W. Hirotaka, L. Shun, D. Manato, H. Yoshio, and A. Hiroshi, J. Appl. Phys. **132**, 145703 (2022).
[42]K. Hossain, A. Tingsuwatit, Z. Alemoush, M. Almohammad, J. Li, J. Y. Lin, and H. X. Jiang, Appl. Phys. Express **17**, 091001 (2024).
[43]Y. Zheng, J. Gao, C. Han, and W. Chen, Cell Rep. Phys. Sci. **2**, 100298 (2021).
[44]Z. Alemoush, N. K. Hossain, A. Tingsuwatit, M. Almohammad, J. Li, J. Y. Lin, and H. X. Jiang, Appl. Phys. Lett. **122**, 012105 (2023).
[45]S. J. Grenadier, A. Maity, J. Li, J. Y. Lin, and H. X. Jiang, Appl. Phys. Lett. **115**, 072108 (2019).